



Characterization of the anisotropic thermal conductivity of additively manufactured components by fused filament fabrication

Ahmed Elkholy¹ · Mahmoud Rouby¹ · Roger Kempers¹

Received: 28 January 2019 / Revised: 8 August 2019 / Accepted: 31 August 2019 / Published online: 12 September 2019
© Springer Nature Switzerland AG 2019

Abstract

Recently, additive manufacturing (AM) has been successfully employed to fabricate heat exchangers due to its ability to create complex geometrical structures with high volumetric-to-area ratio, which can be designed to increase convective heat transfer from surfaces. Fused filament fabrication (FFF) is one of the most popular AM methods due to its accessibility and low-cost hardware. The effect of process parameters on the mechanical properties of FFF 3D-printed parts has been studied extensively. However, there are limited reliable data for the thermal conductivity of 3D-printed components which has impeded the development of additively manufactured heat exchangers. In the current study, the effect of the layer height and raster width have been investigated experimentally and numerically to characterize the effective thermal conductivity of 3D-printed components and investigate the thermal anisotropic nature of unidirectional printed parts. The results showed that increasing the layer height and width causes deterioration in the effective thermal conductivity of up to 65% of the pure polymer. In addition, the thermal conductivity was measured for a range of PLA composites and it was found that their anisotropic ratio can be as high as 2. The unidirectional effective conductivity model was subsequently modified to characterize the common cross-hatched layer fill configuration, and the influence of fill ratio on the effective thermal conductivity was investigated. Finally, the effective thermal conductivity of several commercially available PLA composite filaments was characterized experimentally.

Keywords Fused filament fabrication · Fused deposition modeling · Printing parameters · Thermal conductivity · PLA · Polymer composite

1 Introduction

Polymers have many advantages for heat exchanger applications, such as corrosion resistance, low weight, and smooth surfaces which can limit fouling. Nevertheless, their low thermal conductivity narrows their application [1]. The addition of conductive fillers inside the polymer matrix is an effective remedy to this issue. Polymer composites are conventionally produced by an injection process [2]. However, controlling the injection process parameters—such as injection flow conditions, filler volume concentration, their distribution, and their orientation state inside the polymer matrix—is not practically achievable.

Additive manufacturing (AM) is an alternative approach to producing end products of composite polymers [3, 4]. It depends on laying the material layer by layer according to the designed 3D CAD model. Compared with subtractive methods, it has many advantages, such as shortening the production time cycle and reducing cost [5, 6]. AM has many techniques such as stereolithography (SLA), fused filament fabrication (FFF) or fused deposition modeling (FDM), selective laser sintering (SLS), and laminated object manufacturing (LOM) [7]. A recent review paper [8] illustrates some novel heat exchanger designs enabled by different methods of AM.

Recent studies have shown the ability to produce final prototypes of polymer heat exchangers using one of the previously mentioned methods. For example, Jia et al. [9] employed the FDM process to produce a heat sink made of a thermally conductive graphite-polymer composite using a 3D printer extruder. Their results showed that it achieved a similar energy dissipation effectiveness compared with the

✉ Roger Kempers
kempers@yorku.ca

¹ Department of Mechanical Engineering, York University,
4700 Keele Street, Toronto M3J 1P3, Canada

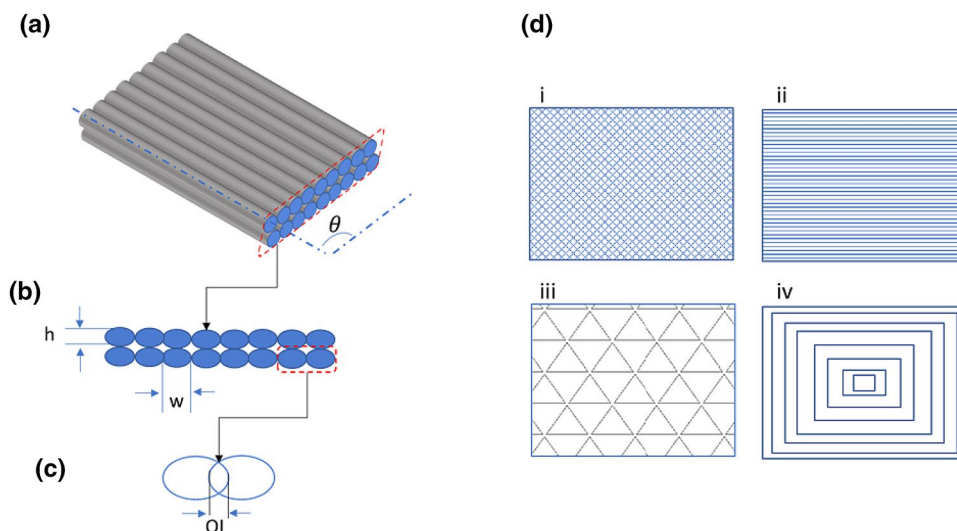
conventional aluminum heat exchanger. In the same direction, Hymas et al. [10] established a new hybrid approach of FDM and embedded metallic strips to fabricate a composite polymer heat exchanger (CPHE). Kalsoom et al. [11] exploited the stereolithography process to produce an electronic heat sink from composite resin made of synthetic diamond fillers and acrylate polymer. In this context, the current work is dedicated to studying the effect of the FDM process parameters on the thermal properties.

FFF (often interchangeably referred to as the trademarked FDM) is one of the most commonly used AM fabrication techniques due to its simplicity, low-cost hardware and feedstock, large open-source development community and wide range of thermoplastic filaments, and no requirement for chemical post-processing. The process involves depositing the molten material layer by layer on a heated bed using a continuous filament of thermoplastic feedstock which passes through a heated nozzle moving in the X – Y plane. The nozzle motion is controlled according to the data generated by slicing software which divides the original CAD model into separate layers. Once one layer is completed, the bed is lowered to begin another, until the component is complete. This process has many parameters, such as layer height, raster width, the overlap between rasters, infill pattern and raster angle, as shown in Fig. 1. Several studies have investigated the influence of these parameters on dimensional accuracy and printing resolution [12–14]. Other work has addressed the influence of these parameters on the mechanical properties of pure polymer using a design of experiment (DOE) approach and the Taguchi method [15–22]. For instance, Cantrell et al. [16] characterized the tensile and shear properties of 3D-printed parts made of acrylonitrile–butadiene–styrene (ABS) and polycarbonate at various raster angles and different build directions. Generally, these

studies demonstrate the anisotropic behavior present in the 3D-printed components that can be altered by changing the printing parameters. Moreover, they show that their mechanical properties are inferior compared with pure polymers due to the air voids generated inside the polymer matrix.

To address these deficiencies, Nikzad et al. [23, 24] found that the mechanical and thermal properties of ABS-printed components could be improved by including metallic filler particles of iron or copper into the FDM filament. They utilized the transient line source technique and differential scanning calorimetry (DSC) to measure thermal conductivity and the thermal capacity of the resultant polymer composite. Their results showed the thermal conductivity improved markedly above 30% volume fraction of filler. However, the thermal capacity deteriorated by incorporating the metallic fillers at any volume percentage. They also examined the dynamic mechanical properties of the printed composites and showed that high filler percentage reduced the material strength due to poor filler distribution, agglomeration, and the development of voids. Hwang et al. [25] examined similar feedstocks and characterized the effect of printing parameters, such as printing temperature and fill density on the mechanical properties of pure ABS. Masood et al. [26] manufactured a nylon–iron FDM filament for direct rapid tooling of injection dies and inserts. Laureto et al. [27] used the guarded heat flow meter TCA300 to quantify the through-plane thermal conductivity of 3D-printed parts made from the commercially available polylactic acid (PLA) filament and its metal composites. They quantified the particles size, their volume fraction, and also the air void fraction using backscattered electron (BSE) microscopic photos; these measurements were employed in three analytical models: Maxwell–Eucken [28], Lichtenecker [29], and Landauer [30], and compared to the experimental

Fig. 1 FFF process parameters: **a** raster angle, θ ; **b** layer height, h , and raster width, w ; **c** overlap, OL ; **d** Infill pattern (i. hatched layers, ii. unidirectional or lines, iii. triangles, iv. concentric)



measurements. It was shown that these models are deficient in predicting the experimental measurements.

Shemelya et al. [31] utilized the Transient Plane Source (TPS) technique to characterize the anisotropic thermal properties of 3D-printed ABS composites filled with graphite, carbon fiber, and silver. Flaata et al. [32] developed a steady-state apparatus designed specifically to measure the thermal conductivity of 3D-printed composites and exploited it to test some feed stock materials available commercially for FDM, such as PLA, ABS, brass PLA, bronze PLA, and stainless-steel PLA. However, there is a large discrepancy between the measured values by Laureto [27], Shemelya et al. [31], and Flaata et al. [32]. For instance, ABS has a thermal conductivity of 0.35 W/mK, according to [32] when it was tested by [31], and suggested to have a value range from 0.15 to 0.2 W/mK, depending on the direction of measurements which represents a deviation of 57–75%. The same discrepancy applies for PLA and its composites. Prajapati et al. [33] studied the effect of the air gap on the anisotropic thermal conductivity ratio for unidirectional FDM 3D-printed parts made from ABS and ULTEM. They utilized a Stratasys Fortus 450mc printer and successfully characterized effective thermal conductivity as a function of the spacing between the rasters. They concluded the anisotropic ratio could reach up to 1.7 for both materials, depending on the air gap between the rasters. However, this printer is not open-source and therefore they had limited control over the process parameters or materials.

The composites in these studies can be classified as discontinuous fiber composites because the fillers exist as discrete particles inside the polymer matrix. Most have demonstrated improved mechanical and thermal properties; however, there are limits to their performance such as porosity generation in the case of metal fillers. Other limitations are associated with the discontinuous nature of the composite, especially at low filler concentrations below the percolation limit, such as the filler distribution and the interfacial heat resistance between the two phases. Generally, filler orientation is not considered to be a problem because Shofner et al. [34] proved that the vapor-grown carbon fibers (VGCFs) are aligned well in the material feedstock and after printing in the FDM traces due to the shear effect happening through the extrusion process. To address these limitations, other researchers have investigated the printing of continuous fiber composites using FDM [35–40]. This process rests on impregnating a continuous filler into the polymer matrix, using a modified nozzle which can liquify the thermoplastic and wrap it around the filler filament while printing.

In summary, while the effects of printing parameters on the mechanical properties of 3D-printed components have been studied extensively, there is a limited understanding of the effective thermal conductivity of 3D-printed components. Development of effective 3D-printed composite

polymer heat exchangers requires an understanding of the anisotropic nature of the printed parts with respect to process variables to produce reliable thermal conductivity data and performance models. Therefore, the objectives of this work are to characterize the effect of geometric printing parameters such as the layer height, raster (road) width, and fill ratio on the anisotropic effective thermal conductivities of FFF-printed components, and to develop and validate numerical models which can be used to further predict thermal performance for other printing configurations and process variables. Other printing parameters such as temperature and print speed have more of an indirect effect on the effective thermal conductivity through their influence on the internal geometry. As such, these parameters were not considered in the current work and only the basic geometry parameters were investigated. A further objective is to characterize the thermal performance of composite FFF feedstocks as they pertain to potential heat transfer applications.

2 Sample design and preparation

A popular infill pattern for printing with FFF or FDM is to print using a cross-hatched layer configuration [41]. This requires printing a layer at an angle and the subsequent one at another angle, most usually perpendicular to it, such as the one shown in Fig. 1di. The effect of the process variables on the anisotropic thermal conductivity of FFF or FDM 3D-printed parts was characterized by first experimentally measuring how these parameters will alter heat transfer within unidirectional printed parts, using this experimental data to validate a numerical model and subsequently using the validated model to characterize thermal conductivity at any angle.

Investigation of the anisotropic nature of unidirectional parts requires specimens of the same size, printed in three different configurations, as shown in Fig. 2. The first is used to quantify the thermal conductivity in the z direction, k_{zz} , the second is for the y direction, k_{yy} , and the third is for the x direction, k_{xx} . In the present study, the first direction, k_{zz} , was printed and measured experimentally and used to validate a numerical model. Numerical and analytical models were subsequently used to characterize thermal conductivity in the other directions. The influence of the layer height was studied by printing the specimens with different values ranging from 0.1 to 0.3 mm, while keeping the raster width and overlap constant at 0.4 mm and zero, respectively, which are the default printer settings. As for the layer width, its value was varied from 0.4 to 0.8 mm while maintaining the layer height and overlap at 0.15 mm and zero. All other process parameters, such as nozzle temperature, speed, etc., were preserved constant as shown in Table 1.

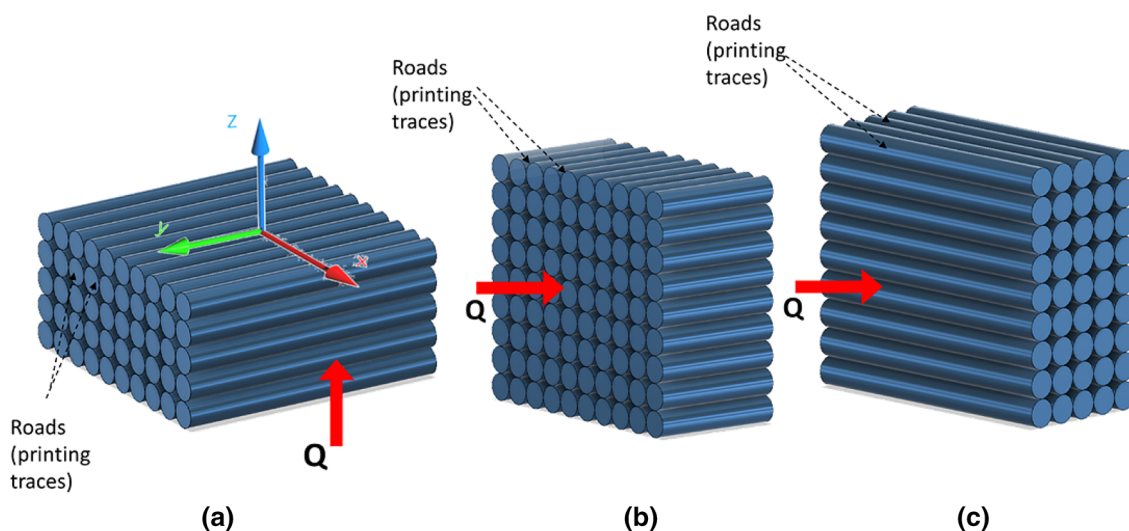


Fig. 2 Different configurations to measure the thermal conductivity in: **a** z direction, k_{zz} , **b** y direction, k_{yy} , **c** x direction, k_{xx}

Table 1 The parameters used to print the samples

Parameter	Value
Sample size	40 mm × 40 mm × 3 mm
Layer height	0.1 mm–0.3 mm
Raster width	0.4 mm–0.8 mm
Overlap	0%
Fill %	100%
Nozzle temperature, T_N	200 °C
Bed temperature, T_b	60 °C
Printing speed, v	60 mm/s
Pattern	Lines

All samples were printed using 100% fill of PLA filament using an Ultimaker® 2 printer. Each sample was printed to the size 40 mm × 40 mm × 3 mm to facilitate thermal conductivity measurement. An automatic ULTRAPOL polishing machine was utilized to ensure that the sample surfaces were parallel and that its surface roughness was very small to minimize thermal contact resistance. The sample surface roughness was measured after polishing at several spots by means of a profilometer (Bruker ContourGT-K). It was found to have an average R_a of $0.912 \pm 0.1 \mu\text{m}$. The sample thickness was measured again at different locations after polishing using a micrometer to quantify any uncertainties in thickness.

Numerical or analytical determination of the thermal conductivity for the other directions requires an investigation of the pattern of layers after printing, which was carried out by means of a microscopic study. Also, this study was used to obtain the air volume fraction inside the matrix. Preparation of the samples for the microscopic study was achieved

by installing them through an epoxy well and letting them cure for a day. Then, they were cut using an abrasive cutting wheel and polished in two sequential steps with silica carbide sandpapers of 180–1200/400 on the same polishing machine.

3 Experimental measurement of effective thermal conductivity

Several methods have been used to measure the thermal conductivity of polymer composites manufactured either by AM or by conventional methods. These include the transient plane source (TPS) technique [31], transient line source for homogeneous molten composite mixture [23], steady state [32], and laser flash method [42]. Laser flash and TPS techniques quantify thermal diffusivity and require additional digital scanning calorimetry DSC measurements to quantify thermal capacity and therefore measure the anisotropic thermal conductivity. Consequently, the apparatus developed in the current work is a steady-state device which can directly measure effective thermal conductivity in all directions.

Oftentimes, steady-state thermal conductivity apparatuses characterize thermal conductivity by sandwiching the sample between two instrumented and calibrated meter bars to measure heat flux through the sample and temperature at the contacting surfaces [43]. These types of apparatuses are typically used to characterize thin, conductive samples. However, for relatively thick, low-conductivity materials, such as those in the present study, it was found that an appreciable fraction of the heat can bypass the sample through the insulation surrounding the bars, thereby limiting measurement accuracy.

To achieve the accurate and precise measurements required to characterize these materials, an apparatus was developed which is based upon a modified guarded hot plate technique outlined in ASTM C177 [44] and is shown schematically in Fig. 3a. A known thermal power from the electrical heaters embedded in the primary heater block was conducted through the sample to a temperature-controlled primary cold block. The resultant steady-state temperature difference across the sample was measured using the resistance temperature detectors (RTDs) embedded in each block and the measured thermal resistance of the sample, R_{meas} , is given by:

$$R_{meas} = \frac{(T_a - T_b)}{Q}, \tag{1}$$

where $(T_a - T_b)$ is the temperature difference across the sample and Q is the measured input electric power to the primary heaters ($P = IV$).

The measured thermal resistance represents the summation of the bulk sample resistance and the thermal contact resistance between the sample and the apparatus is given by:

$$R_{meas} = R_{c,1} + R_{c,2} + R_{sample} = R_c + R_{sample} \tag{2}$$

$$= R_c + \frac{L}{k_{sample}A}, \tag{3}$$

where $R_{c,1}$ is the contact resistance between the sample and the primary heater, while $R_{c,2}$ is the contact resistance between the sample and the primary cooler.

The thermal conductivity of the sample can be calculated by rearranging this as:

$$k_{sample} = \frac{L}{A \left[\frac{(T_a - T_b)}{Q} - R_c \right]}, \tag{4}$$

where, L is the specimen thickness and A is the sample cross-section area.

The contact resistance was obtained by measuring the total thermal resistance for several samples with the same surface conditions and different thicknesses, and then fitting the measured values against the samples' thicknesses to obtain the y intercept.

The key elements in designing an accurate, guarded, steady-state method rest on creating two hot-and-cold isothermal plates and ensuring all supplied and measured input power flows through the sample. This was achieved by guarding the heat source with another independent secondary heater block which surrounds the primary block whose temperature was controlled to be identical to the primary heater block. By ensuring identical temperatures between the primary and secondary (guard) heater blocks, the heat going through the sample can be quantified by measuring the electric power to the primary heater block. Similarly, the cold plate was guarded from its top surface by another secondary cooling block, as shown in Fig. 3a.

Numerical simulations were carried out to design the primary and secondary heating and cooling blocks, to ensure all primary heater input power flowed through the sample, and to quantify any heat loss when measuring relatively low conductivity materials. Overall, for representative operating conditions and sample properties, thermal simulations demonstrated that over 99% of the input power to the primary heater block flowed through the sample and that the surface

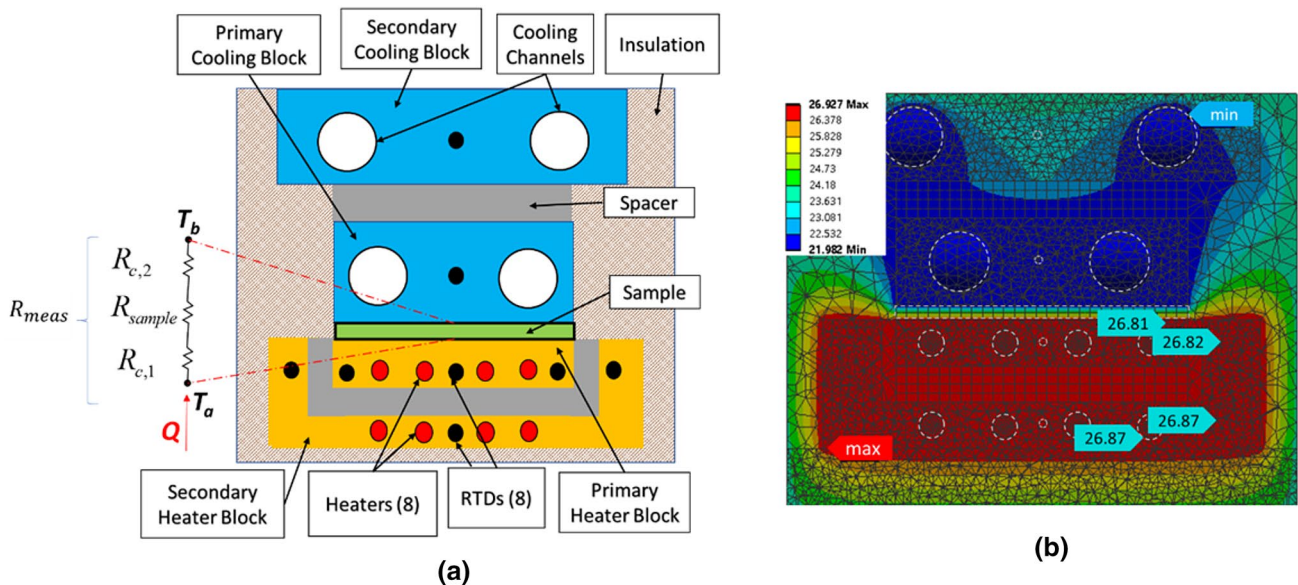


Fig. 3 a Schematic of experimental apparatus. b Numerical simulation of the experimental apparatus

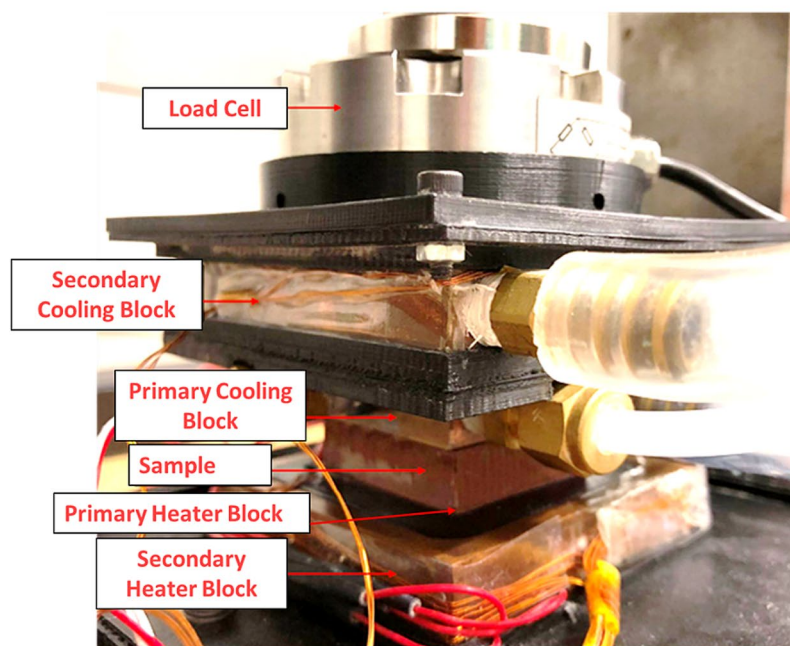
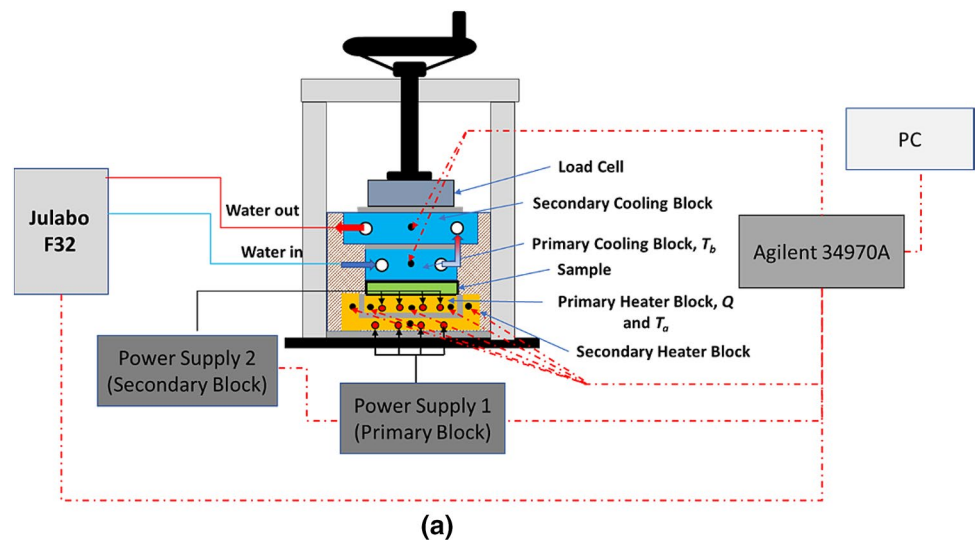
temperatures of the hot and cold blocks were isothermal to within 0.04 K, as shown in Fig. 3b. Also, the temperature difference between the primary and secondary blocks was about 0.06 K, as shown in Fig. 3b.

The overall experimental setup is shown in Fig. 4a. The primary and secondary (guard) blocks were machined from copper because of its high thermal conductivity to help ensure uniform temperature within each block. The primary heater block was 40 mm × 40 mm × 6.35 mm. Four cartridge heaters (Sun Electric Heater), with a diameter of 3.1 mm (1/8 inch) and a length of 38 mm (1.5 in), were inserted into holes drilled through the block. The secondary heater block had overall dimensions of 70 mm × 70 mm × 15.7 mm and

had a 55 mm × 55 mm × 9.35 mm cutout, into which a plastic spacer and the primary heater block were inserted. An additional four 3.1 mm × 50 mm (1/8-inch × 2 inches) cartridge heaters were installed into the secondary heater block.

The temperature of each block was measured using three RTDs 1 mm × 15 mm (Omega, 1PT100KN1510) inserted into holes at the locations shown in Fig. 3 such that each sensor from the primary block was opposite a corresponding sensor on the secondary heater block. The input power to each block was supplied using two independent DC supplies (Aim TTI, CPX400D) and controlled by varying the supplied voltage.

Fig. 4 Experimental apparatus: **a** overall schematic. **b** Photograph of test section



(b)

The primary cooling block measured 40 mm × 40 mm × 12 mm, while the secondary block was 80 mm × 80 mm × 12 mm. Each was drilled with 8.5 mm diameter holes in a U-channel configuration to permit cooling water to flow through them. Temperature-controlled water supplied from a circulator (Julabo F32-HE) flowed through the primary block and then to the secondary one. Both blocks had a single RTD inserted near the center to monitor block temperatures. An additional RTD was inserted in the water channel to provide feedback to the circulator. During testing, the chiller temperature was tuned to keep the

3.1 Uncertainty analysis

The resulting uncertainty in measuring the thermal conductivity was a combination of two types: device bias uncertainty and the precision uncertainty. The bias uncertainty of the device was predicted by the error propagation method detailed in [45]. The uncertainties for all input parameters are shown in Table 2 and the precision uncertainty was determined by repeating the measurement three times using the same device under the same conditions. The maximum uncertainty originating from the repeatability test was less than 1.8%.

$$U_k = \sqrt{\left(\frac{\partial k}{\partial V} U_V\right)^2 + \left(\frac{\partial I}{\partial I} U_I\right)^2 + \left(\frac{\partial k}{\partial L} U_L\right)^2 + \left(\frac{\partial k}{\partial T} U_T\right)^2 + \left(\frac{\partial k}{\partial A} U_A\right)^2} \tag{5}$$

sample average temperature close to the ambient temperature to minimize the heat loss or gain from or to the sample side walls. The heat loss was further estimated using the numerical simulation and was found to be less than 2% of the input power to the primary heater. The function of the secondary cooling block was to help isolate the system from temperature fluctuations in the surrounding environment.

The sample under test was clamped between the primary and secondary heating and cooling blocks using a clamping screw, device frame, and the load cell (AST, KAF-S/500/0.1), as shown in Fig. 4. Samples were clamped with a pressure of approximately 3 bars and a few droplets of thermal paste (ARCTIC, MX-4) were used to minimize thermal contact resistance and to help ensure reparability of results.

The entire assembly was encased in silica aerogel insulating material with a thermal conductivity of 0.014 W/mK. The ambient temperature was monitored using a T-type thermocouple.

Once assembled into the heater blocks, the RTDs were simultaneously calibrated together using a 50 mm-long Fluke PRT full immersion reference probe (Model 5606), which was certified from − 200 to 160 °C. The calibration was carried out using an isothermal-controlled copper chamber from 5 to 30 °C using the approach described in [43]. Upon calibration, the uncertainty in temperature difference between the sensors was ± 0.012 K.

The temperature sensors were monitored using an Agilent 34970A data acquisition system, while the input power to the primary heater block of the heater side was carried out by measuring the voltage and current using independent Agilent 34401A digital multimeters. A MATLAB script was used for log measurements and control the secondary heater block power. The criteria for secondary power control were to ensure the temperature difference between the primary and secondary heater blocks did not exceed 0.01 K at steady state. The system was considered steady state when the time gradient of the temperature for each sensor was less than 1e−5 K/s.

where V is the applied voltage and I is the resultant current which was utilized to obtain the imposed heater power.

4 Numerical modeling

The effective thermal conductivity of the printed components in z or x directions was modeled numerically by simplifying the geometry into a 2D cross-section and extracting unit-cells to represent the overall geometry as shown in Fig. 5. Although the sample’s microstructure was not perfectly symmetric, and some of the unit-cells or rasters were inconsistent, this simplification allowed for relatively straightforward numerical modeling of the effective thermal conductivity of the structure. The unit-cell had a dimension of $h/2$ in the z direction and $w/2$ in the x direction, as shown in Fig. 5a.

Table 2 Uncertainties for the measured quantities of the experimental device

Parameter	Uncertainty	
Sample thickness, L	0.15 mm (maximum)	
Sample area, A	1×10^{-5} (m ²)	
Temperature difference	0.012 K	
Voltage	Range	± (% of reading + % of range)
	100 mV	0.0050 + 0.0035
	1 V	0.0040 + 0.0007
	10 V	0.0035 + 0.0005
	100 V	0.0045 + 0.0006
Current	10 mA	0.050 + 0.020
	100 mA	0.050 + 0.005
	1 A	0.100 + 0.010

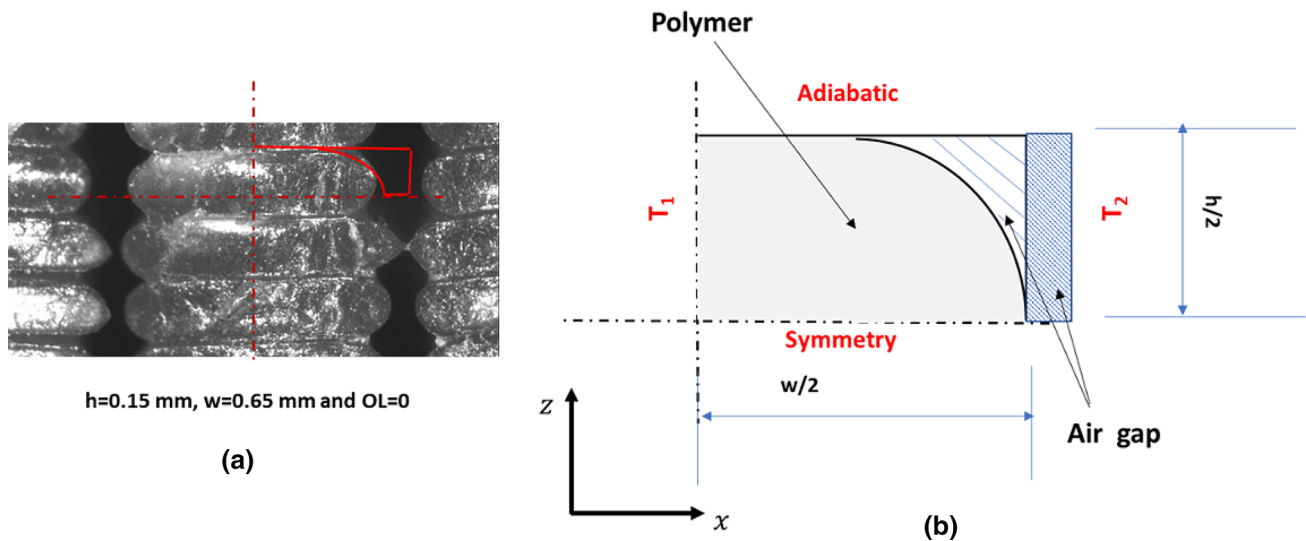


Fig. 5 Numerical model: **a** unit-cell **b** domain and boundary conditions

ANSYS Fluent 18.2 software [46] was used to model the conduction heat flow through printed parts. The numerical model required inputting the thermal conductivity of pure polymer, which was measured by printing a sample with a small layer height of 0.06 mm and a high percentage of overlap to ensure that there were no air gaps generated inside the part; this was found to be 0.2207 W/mK. The air standard thermal conductivity was defined as 0.0242 W/mK.

Due to the repeating nature of the geometry, only a single unit-cell as shown in Fig. 5b was modeled with the appropriate boundary conditions:

- A temperature difference boundary condition was applied at the right and left boundaries of the domain to establish heat flow through the sample. The temperature difference, $T_1 - T_2$, was set equal to 1 for all cases.
- Adiabatic and symmetry conditions were imposed for the top and bottom boundaries to ensure heat flows through unit-cell the x direction, as shown in Fig. 5b. The symmetry type boundary was assumed based on the geometry simplifications of the unit-cell. The adiabatic conditions (which is also symmetric) ensure heat flows through the unit-cell in the same direction measured experimentally.

The effective thermal conductivity was then calculated in x direction, k_{xx} , by solving the energy equation and quantifying the heat transfer rate in that direction. Fourier's law can then be applied to calculate the effective thermal conductivity of the unit-cell. For effective thermal conductivity in the z direction, the boundary conditions were reversed, and the temperature difference was imposed in the direction of the thermal conductivity being calculated.

The domain was divided into discrete quadrilateral control volumes and the energy equation was solved iteratively. The number of cells was increased from 1093 to 1,666,257 to ensure grid independence. The domain was initialized with a constant temperature of 300 K. The mesh quality was measured using the maximum aspect ratio and the maximum skewness, which were 6 and 0.8, respectively. Convergence was ensured by setting the residuals equal to $1e-10$.

The geometry was varied according to the measured cross-sections and the volume fraction calculated by weighing the samples in the previous section, which was used to determine the air gap distance between the roads.

5 Results and discussion

5.1 Microscopic imaging results and sample characterization

A cross-section of a unidirectionally printed sample is shown in Fig. 6a which depicts the effect of changing the layer height from 0.15 to 0.3 mm, while keeping its width at the default value of 0.4 mm. Here, increasing layer height results in an increase in the air volume fraction within the printed component. A similar effect is apparent when increasing the raster width, as shown in Fig. 6b, where layer height was held constant at 0.15 mm. We can also see from Fig. 6 that the pattern is mostly homogeneous except for some roads which are not connected to each other. This phenomenon is more likely to occur at small layer heights. We conjecture this is because the molten polymer, when unconstrained, preferentially flows to either one side or the other. Another important feature to note

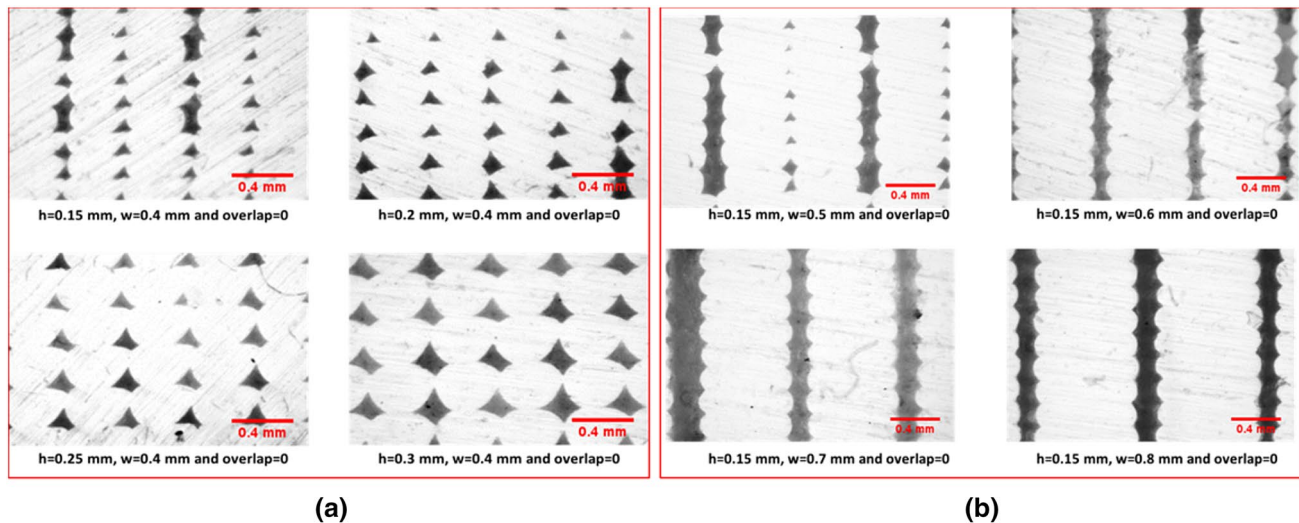


Fig. 6 Microscopic photos showing the effect of **a** layer height, *h*, and **b** raster width, *w*

in Fig. 6 is that the roads begin to completely disconnect for raster widths greater than 0.5 mm.

The volume fraction for each sample was quantified using two approaches. In the first, each photo was converted into an 8-bit image type to allow thresholding. ImageJ software was employed to carry out the thresholding and calculate the air volume fraction. The second approach to quantifying air volume fraction was accomplished by weighing the sample while postulating that the air mass within the part to be negligible and then applying the following equation:

$$v_f = \frac{v_s - v_p}{v_s} \tag{6}$$

where

$$v_p = \frac{m_s}{\rho}, \tag{7}$$

and where v_f , v_p , v_s are the volume fraction of air, the volume that the polymer occupies inside the printed part, and the printed part volume, respectively. ρ is the polymer density which was measured for the PLA filament feedstock.

Tables 3 and 4 show a comparison between the air volume fraction resulting from the ImageJ method and weighing method. As can be seen from these tables, there is a large deviation between the two methods, especially for the layer height. We suspect this is due to the fact that the sample under the microscope represents only one cross-section and the photo was captured for part of this section which may not be representative of the whole sample, especially in cases where the layers are somewhat disconnected. The volume fraction measurements were not consistent between different cross sections; even changing the measurement spot for the

Table 3 Air volume fraction at different layer heights at a constant raster width of 0.4 mm

Layer height, <i>h</i> (mm)	Air volume fraction %		
	ImageJ v_f %	Weighing method	
		v_f %	Uncertainty %
0.15	4.1	11.7	0.14
0.2	6.5	13.5	0.135
0.25	9.8	14.1	0.134
0.3	14.3	15.92	0.131

Table 4 Air volume fraction at different raster widths at constant layer height of 0.15 mm

Raster width, <i>W</i> (mm)	Air volume fraction %		
	ImageJ v_f %	Weighing method	
		v_f %	Uncertainty %
0.4	4.1	11.7	0.137
0.5	11.9	13.7	0.134
0.6	13.7	15.3	0.131
0.7	17.1	19	0.126
0.8	18.1	24.5	0.117

same cross section resulted in different volume fractions. Therefore, the weighing method was used to quantify air volume fractions; we believe this better represents the true value of the parts characterized here. However, the photos give a better insight into the internal geometries and served to inform the geometries used when developing the numerical model.

5.2 Numerical model validation

The thermal conductivity in the z direction, k_{zz} , was measured experimentally and compared with the numerical model, as shown in Figs. 7 and 8. The experimental results, depicted in Fig. 7, indicate that increasing the layer height reduces the thermal conductivity in the z direction until it reaches a value of 0.133 W/mK at a layer height of 0.3 mm due to the increase of air volume fraction. This represents a percentage of reduction of about 40% compared with pure PLA polymer. The thermal conductivity in the z direction, k_{zz} , also decreased with increasing raster width and resulted in a 14% reduction of thermal conductivity at a raster width of 0.8 mm, as shown in Fig. 8.

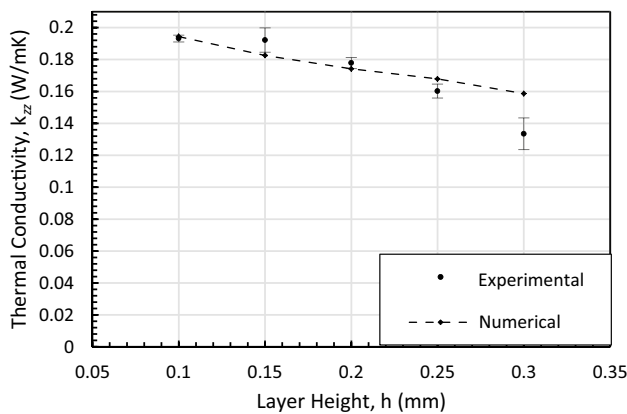


Fig. 7 Comparison between the experimental results and numerical model for studying the effect of layer height on the thermal conductivity, k_{zz} , of unidirectional 3D-printed part at a constant raster width of 0.4 mm

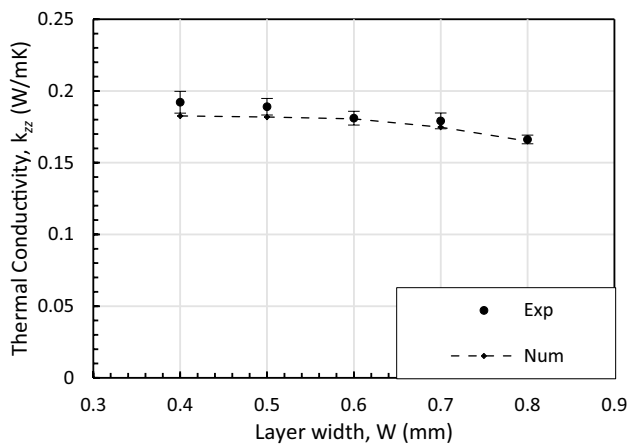


Fig. 8 Comparison between the experimental results and numerical model for studying the effect of raster width on the thermal conductivity, k_{zz} , of unidirectional 3D-printed part at a constant layer raster of 0.15 mm

Overall, the numerical model predictions are in good agreement with the experimental results and predict the effective thermal conductivity to within 5% for 90% of the data points. The model further captures the trend in the change in thermal conductivity with layer height and width. Slight deviations occur at the largest layer height and the lowest layer width. This is likely due to the simplification of a slightly more complex cross-sectional geometry for these cases into the more idealized shapes which were used as representative unit-cells in the numerical model. In addition, in these cases there exists a greater degree of variability in cross-sections used for geometry input to the numerical model; i.e., sometimes the roads are connected and sometimes they were not, as discussed the previous section.

5.3 Effect of layer height

Once the numerical model was established for the relatively complex geometry associated with the z direction (k_{zz}), this was subsequently used to characterize the effect of printing parameters in the x direction (k_{xx}). Thermal conductivity in z - and x -directions depends on the raster shape; however, for the relatively straightforward geometry in the y direction, an analytical parallel model was employed to model the effective thermal conductivity, k_{yy} , given by

$$k_{yy} = (1 - v_f)k_m + v_fk_a, \tag{8}$$

where k_{yy} is the effective thermal conductivity in the y direction, while k_m and k_a are the conductivities for the matrix and air, respectively. v_f is the air volume fraction inside the PLA matrix, which was measured and tabulated in Tables 3 and 4.

The effect of layer height on the thermal conductivity of unidirectional parts in all directions is shown in Fig. 9, along with the experimental measurements in all directions for a layer height of 0.15 mm, as a validation for the other directions. However, as discussed before above, the deviation

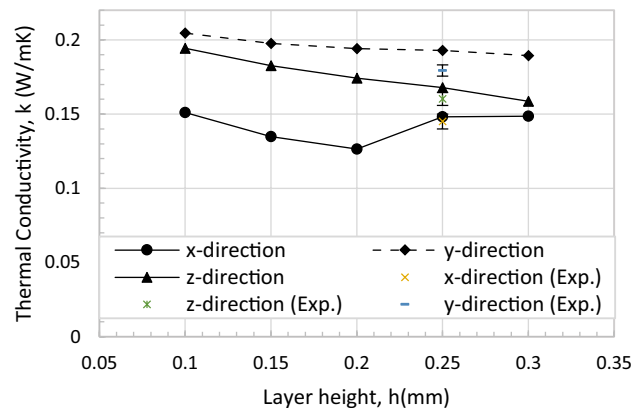


Fig. 9 The effect of layer height on the thermal conductivity for all directions at a constant layer height of 0.15 mm

of the numerical prediction from the experimental measurements is different for all directions, which pertains to the layer disconnection problems that affect the numerical model accuracy differently.

The numerical predictions show that the effect of layer height is more significant in z and x directions, while it is nearly constant for the y direction. The thermal conductivities are higher in z and y directions than for x direction. This is because the heat path in x direction is a series which increases the overall thermal resistance, while it is parallel for the other directions. For the x direction, the thermal

conductivity initially decreases and increases again. This is because, when the layer height is small, the layers are not connected. In summary, the layer height increase causes a decrease in the thermal conductivity, which reaches values of reduction of 42%, 14%, and 28% for x , y , and z , respectively, compared with the pure polymer at a layer height of 0.3 mm. The previous percentages were calculated based on the numerical model predictions.

5.4 The effect of raster width

The influence of the raster width on thermal conductivity in x and z directions was predicted numerically while the parallel model was employed for y direction, as shown in Fig. 10. Like the layer height, increasing the raster width also causes a decrease in thermal conductivity in all directions. The thermal conductivity in y direction is higher compared with other directions for the height effect in Fig. 9 and for the layer width in Fig. 10. The reason behind this can be explained with the help of the corresponding thermal network in Fig. 11. Here, the heat flow direction in y direction is parallel in the air and polymer phases, while it is series in x direction and partly parallel in z direction. For this reason, it can be expected that the thermal conductivity in y direction should be the highest, followed by z direction, and then, lastly, x direction.

The raster width has a severe effect on the thermal conductivity in x direction because the layers are completely disconnected in that direction. The thermal conductivity

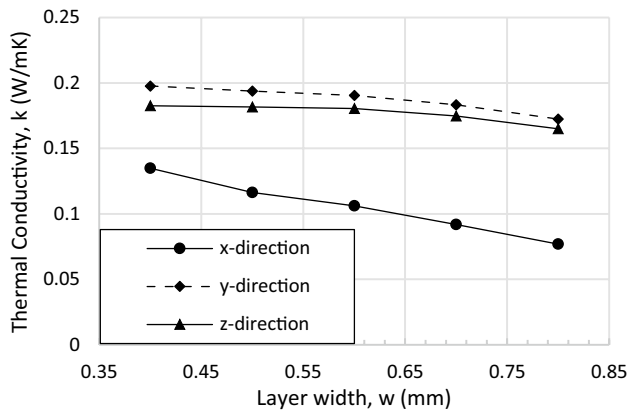


Fig. 10 The effect of raster width on the thermal anisotropic nature of 3D-printed parts

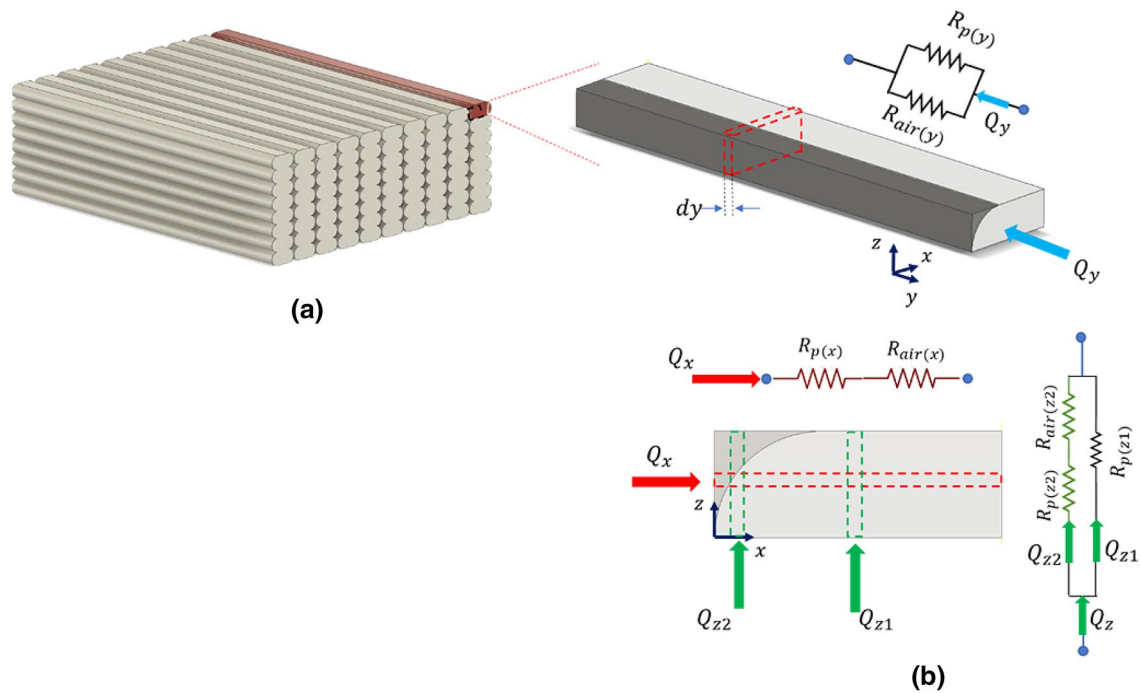


Fig. 11 The equivalent thermal network for the printed part unit-cell: **a** schematic of the printed part **b** thermal network in all directions

in x direction reaches a low thermal conductivity value of 0.077 W/mK at a width of 0.8 mm, which represents a 65% reduction compared with pure polymer, while the reduction is 28% and 25% for y and z directions, respectively. This highlights the importance of characterizing these parameters and demonstrates the possibility of tailoring the thermal properties of the printed parts, especially when printing continuous carbon fiber or low-melting-temperature metals.

5.5 Thermal conductivity modeling for printing at cross-hatched layer configuration

The effect of raster width and layer height on the thermal conductivity of unidirectional 3D-printed parts has thus far been characterized. These data are used here as the baseline to build a general model that can predict the thermal conductivity in x and y directions for bi-directional samples or for samples printed at a cross-hatched layer configuration at any angle, as illustrated in Fig. 12. The thermal conductivity for bi-directional samples was predicted by taking a plane perpendicular to z direction and applying the same boundary condition as that used in Sect. 4. This depends on inputting the thermal conductivity at the principal axes along with the printing angle to predict the heat transfer rate at the general axes which can be used to obtain the corresponding thermal conductivities.

Following the unit-cell modeling approach described previously, Fig. 13 shows the simulated temperature contours for a sample of results at a printing angle of 45° . The input thermal conductivities were 0.197 W/mK and 0.1348 W/mK for principal axes y and x , respectively, which were predicted before at a layer height of 0.15 mm and 0.4 mm for the unidirectional sample in Sect. 5.2. The thermal conductivity for bi-directional samples in the z direction will be very close to their unidirectional counterparts because the contact area between the layers has not change significantly. However, thermal conductivity varies for samples printed using the cross-hatched layer configuration. Figure 14 shows the thermal conductivity in the general axes, x and y for bi-directional samples while changing the printing angle from 0° to 90° . The layers for the last sample type, shown in Fig. 12c, can be interpreted as many bi-directional samples connected in parallel with heat being conducted in the x or y directions. Hence, such types of samples are modelled using the conventional parallel model and the input thermal conductivity for each layer can be extracted from Fig. 14 as a bi-directional sample. Since half of the layer is printed at θ_1 and the other half is printed at θ_2 , only two resistances are required to model the effective thermal conductivity in both directions, as shown in Fig. 15.

As discussed previously, the thermal conductivity in the z direction for such samples are different compared with unidirectional or bi-directional samples; therefore, different

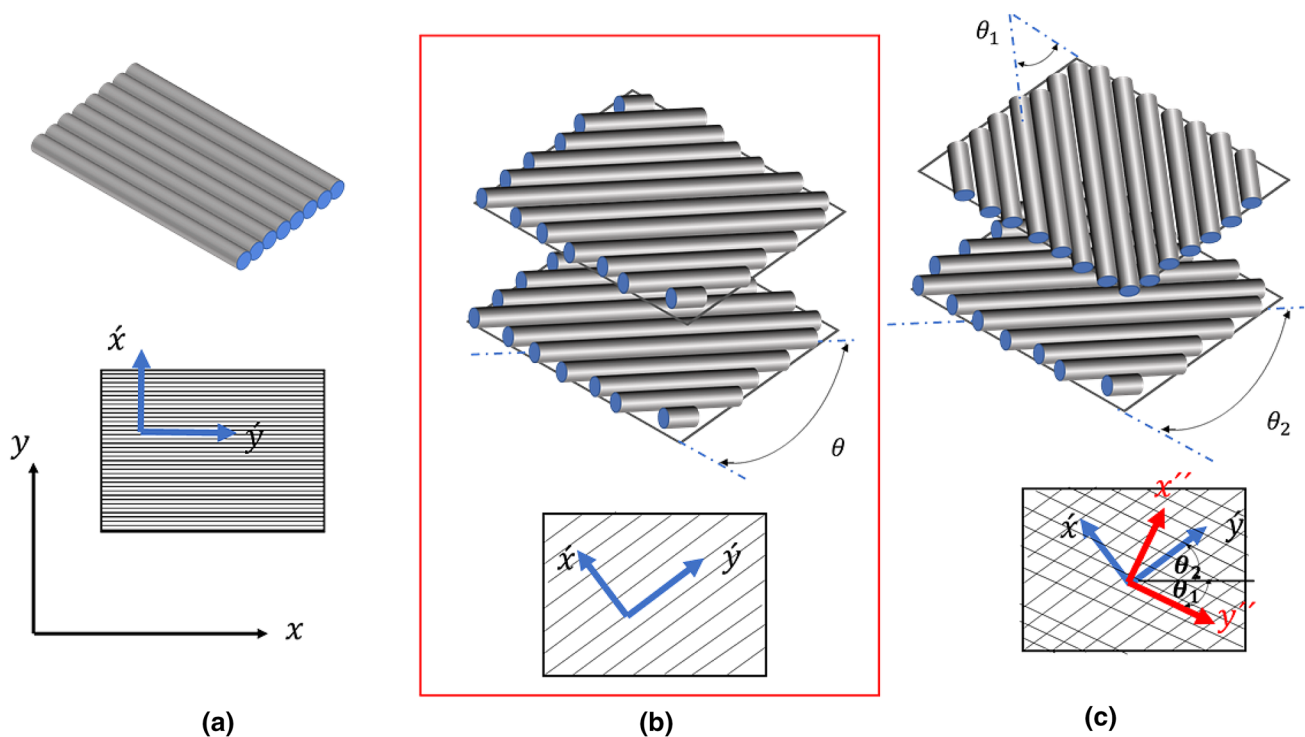


Fig. 12 Thermal conductivity models: **a** unidirectional sample, **b** bi-directional sample **c** cross-hatched layer sample

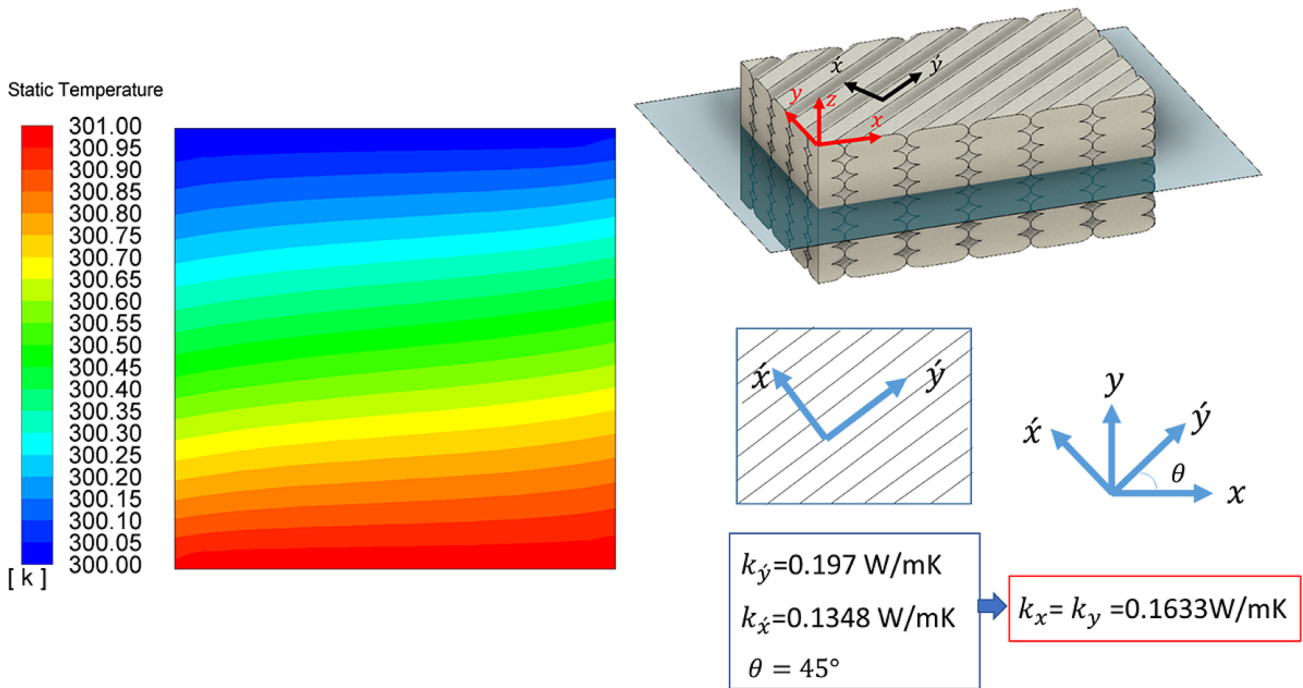
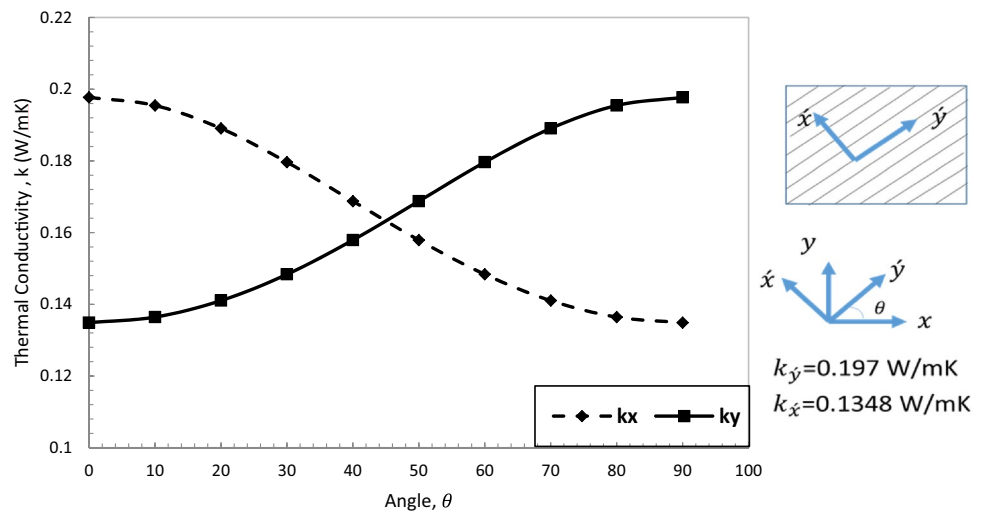


Fig. 13 Temperature contours for a bi-directional sample at printing angle of 45°

Fig. 14 The effect of changing the printing angle on the thermal conductivity in x and y directions for cross-hatched layer configuration



angle combinations were examined—[20°, 70°], [30°, 60°], [45°, -45°], [0°, 90°]—as shown in Fig. 16. The thermal conductivity was similar for the last two combinations because the contact area between the polymer traces through the layers was approximately the same for both. Printing at cross-hatched layer configuration makes the polymer traces though the z direction connected at individual spots instead of having a continuous area of contact. Therefore, all the combinations in this direction were less conductive, compared with the unidirectional sample.

5.6 Effect of fill ratio

The last important parameter to be studied was the fill ratio; this is the polymer volume percentage relative to the part volume. Five samples were printed and tested from pure PLA at 45°/–45° angles with different polymer percentages ranging from 30 to 100%. Figure 17 shows the fill ratio effect on the effective thermal conductivity in z direction. The dash line in this figure represents the thermal conductivity of the pure polymer. The 100% fill

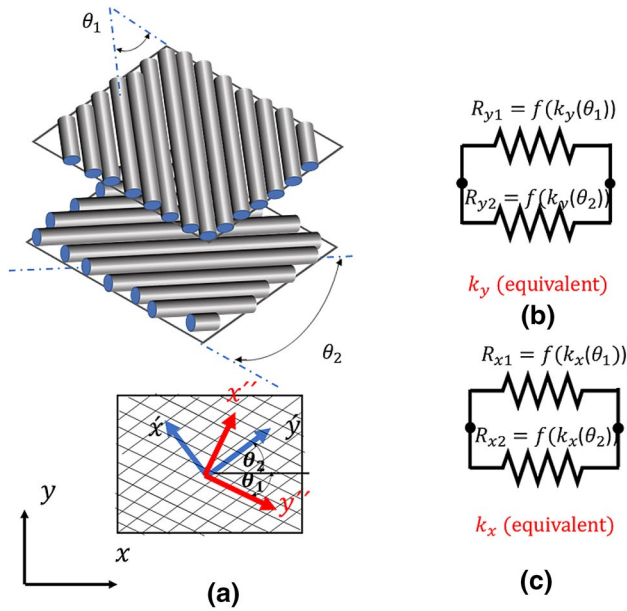


Fig. 15 Thermal conductivity modeling for cross-hatched layer sample in x and y directions

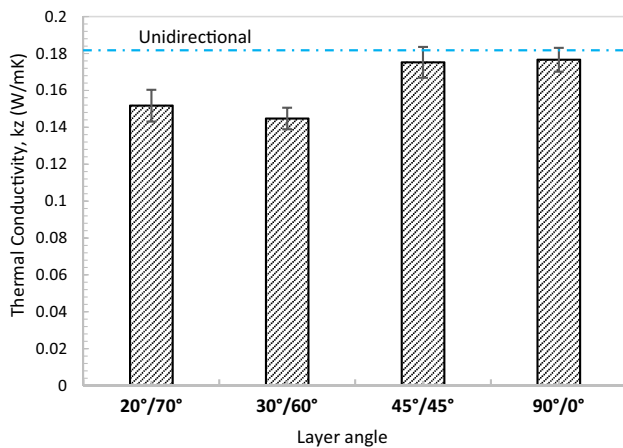


Fig. 16 Thermal conductivity in z direction for cross-hatched layer sample

sample had a lower thermal conductivity compared with pure polymer due to the generated voids between rasters, as discussed previously in Sect. 5.2. Decreasing the fill ratio has a negative impact on the thermal conductivity in the z direction, which can reach up to 63% reduction compared with 100%, and 70% reduction compared to pure polymer due to air volume fraction increase.

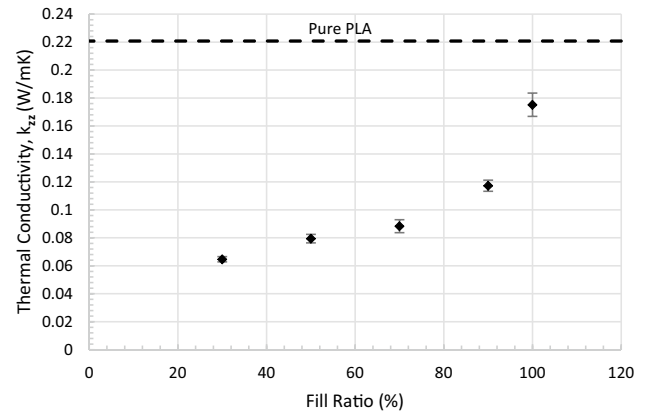


Fig. 17 Effect of fill ratio on the thermal conductivity in z direction for pure PLA

Table 5 Materials' specifications

Filament	Supplier	Filler fraction (%)
Pure PLA	Filaments.ca	0
Metal composites (aluminum, copper, bronze, brass)	Sainsmart	20% (volume-based)
Carbon fiber (Robo 3D)	Robo3d	Unknown
Carbon fiber (Protopasta)	Proto-pasta	< 14.25 (weight-based)

5.7 Polymer composite

The effective thermal conductivity of several commercially available PLA composite filaments was characterized experimentally by printing unidirectional samples at a layer height of 0.15 mm and raster width of 0.4 mm. Four metal PLA composite filaments were purchased from Sainsmart with different filler types; bronze, brass, copper, and aluminum. Two additional carbon fiber composite filaments (from Robo3D [47] and Proto-Pasta [48]) were measured. Table 5 shows the specifications for each filament.

The samples were prepared in the same manner as shown previously in Sect. 2. It was postulated that thermal conductivity in printing direction (y direction) should be higher than the other directions because the fillers tend to align in the direction of the raster [34] and this may help increase filler connectivity. The thermal conductivity was measured in the y and z directions for these composites and compared with pure PLA, as shown in Figs. 18 and 19. To help interpret these results, the samples were sectioned in two different planes to understand filler distribution in the rasters subsequent to printing. A cross-section of the y direction is shown in Fig. 20 and another a perpendicular cross-section of the x direction is shown in Fig. 21.

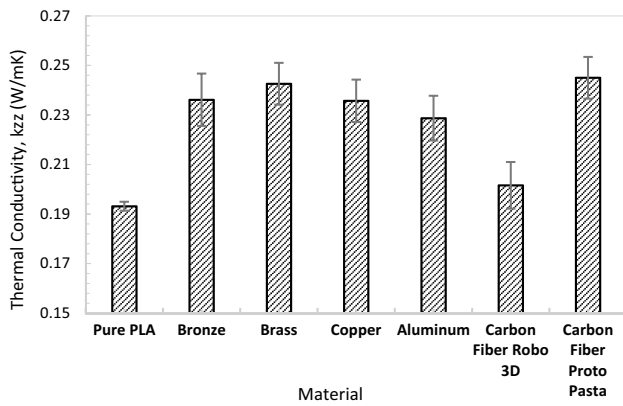


Fig. 18 Thermal conductivity in z direction for several PLA composites

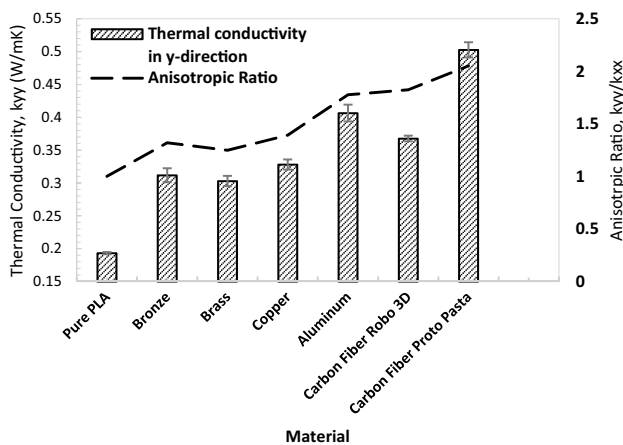


Fig. 19 Thermal conductivity in y direction for several PLA composites

As can be seen in Fig. 18, the thermal conductivity in the z direction for metallic composites is relatively similar, irrespective of filler type, which indicates that the fillers are poorly connected in the z direction. This imposes a huge thermal interface resistance between the filler and the matrix, compared with the filler resistance, and this indicates that the filler concentration is small and did not reach the percolation limit wherein the fillers form a connected network through the matrix [29]. The carbon fiber composite (Proto-Pasta) has the highest thermal conductivity which represents approximately a 26% increase in thermal conductivity over pure PLA. The carbon fibers inside the matrix are clearly seen to have a cylindrical surface inside the matrix, especially for the Robo3D sample (Fig. 21).

Another factor that plays a significant role in reducing the thermal conductivity in this direction, besides filler discontinuity, is the porosity generation inside the printed traces, as highlighted by red circles in Fig. 20. In the printing

direction, y direction, the thermal conductivity showed a reasonable increase for all the samples, especially in the case of carbon fiber which reached up to 162% compared with pure PLA because the extrusion through the nozzle helped to orient the fillers. This illustrates that the carbon fibers are partially connected compared with the metallic fillers; this is clearly shown in Fig. 21.

Although the thermal conductivity of metallic fillers is different, there is virtually no corresponding effect on the effective thermal conductivity of the printed composite. This is because the effective thermal conductivity is not only affected by the thermal conductivity of the fillers, but there are some other factors that play an important role, such as how the fillers are connected, fillers shape, their distribution, their orientation, contact resistance between the two phases, and the resulting voids originating from the filament fabrication. We conjecture that the aluminum composite had a higher thermal conductivity in y direction despite having lower filler thermal conductivity than copper for one of the above-mentioned reasons.

Post processing techniques such as vapor finish for polymer or sintering for composite filaments can help in boosting the thermal conductivity. Sintering the printed composite part can help to connect the fillers to each other, forming a network of conductive paths for heat flow. Ebrahimi et al. [49] studied the sintering effect on the thermal conductivity only for copper composite. It was demonstrated that sintering improved the effective thermal conductivity by an order of magnitude compared with non-sintered samples.

Vapor finishing techniques can be used to smooth outer surfaces of the printed parts and could serve to help lower thermal contact resistance with adjacent components; however, it is unclear what affect this would have on the interior geometry and thus the effective thermal conductivity of the printed parts.

6 Summary and conclusions

This work examined the influence of FFF process parameters on the anisotropic thermal properties of unidirectional 3D-printed parts. An experimental facility was developed to measure the effect of the layer height and raster width on the thermal conductivity in the z direction and to validate a numerical model which was subsequently used, along with an analytical model, to characterize the thermal conductivities in all directions for the unidirectional 3D-printed parts. The thermal performance of the unidirectional samples was used as a baseline data set to construct a general model able to predict the conductivity of cross-hatched layer configuration at any angle, in addition to investigating the infill ratio effect for this configuration. These modeling approaches can be applied and extended to other 3D-printed geometries

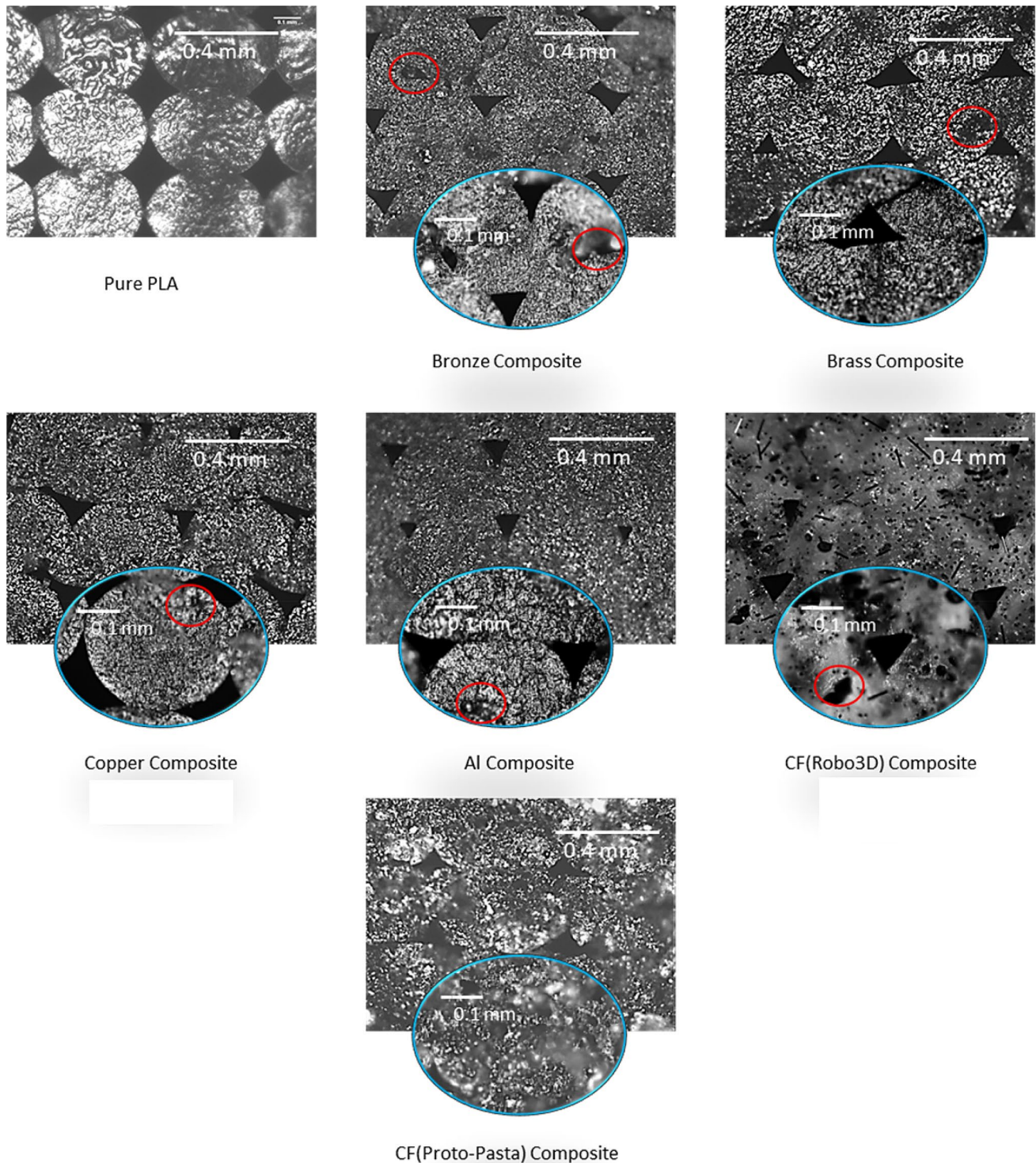


Fig. 20 Microscopic images for several PLA composites perpendicular to y direction

or composite printing techniques, especially those which achieve improved effective thermal conductivities such as continuous wire printing [35, 36], continuous fiber-reinforced composite [37, 38], or low melting temperature metals [50] which are all based upon FFF and show good

potential for a range of heat exchange applications. Lastly, we examined the anisotropic ratio for some of the commercially available polymer composite filaments also printed in a unidirectional form. The main outcomes can be summarized in the following points:

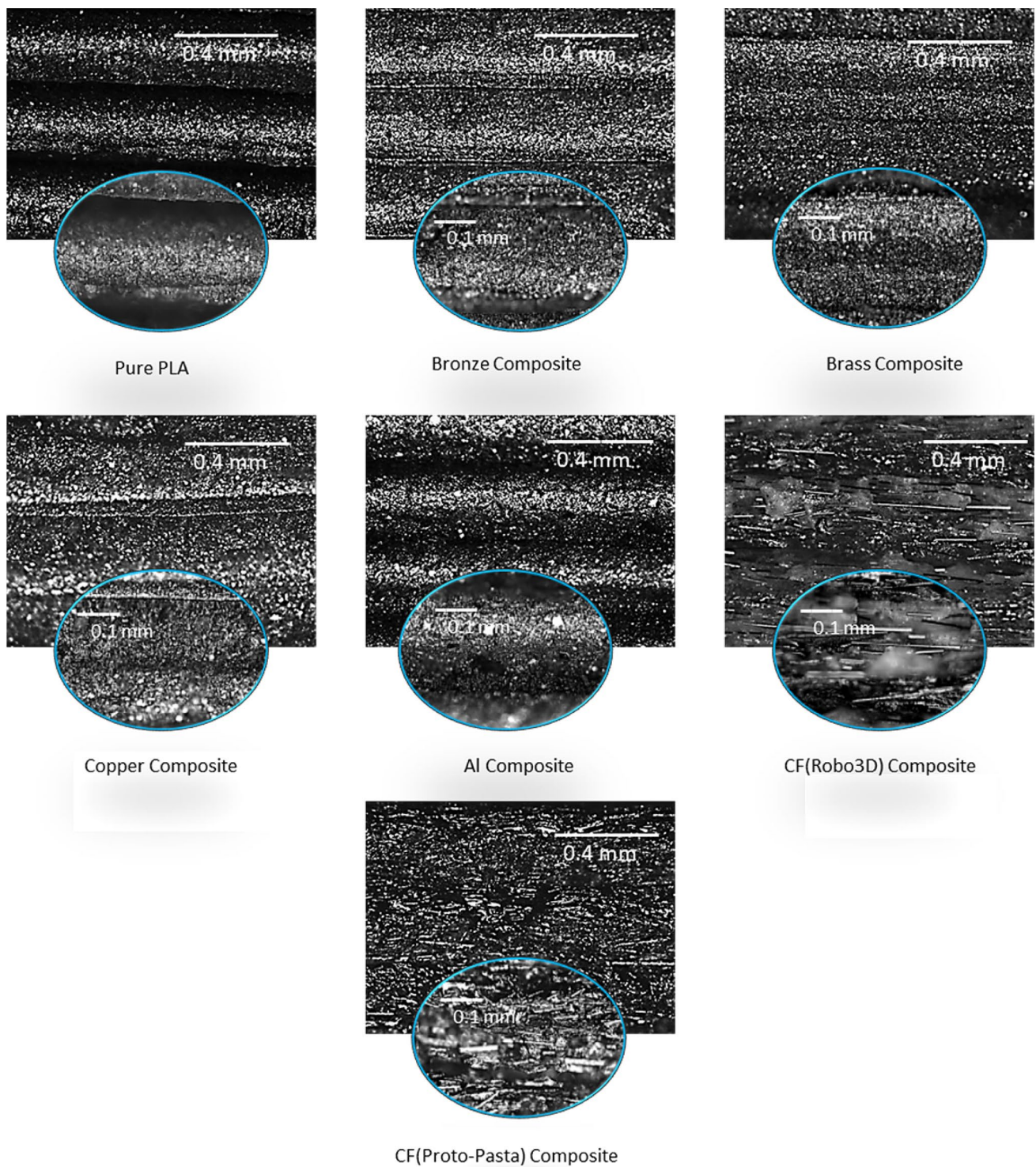


Fig. 21 Microscopic images for several PLA composites perpendicular to x direction

- Increasing either the layer height or raster width reduces thermal conductivity in all directions as a result of porosity generation.
- The effect of raster width is more significant than the layer height, especially when a layer disconnection problem exists.

- Increasing the layer height while keeping the raster width constant at 0.4 mm results in a drop in the thermal conductivity which reaches values of 42%, 14%, and 28% reduction in x , y , and z directions, respectively, at a layer height of 0.3 mm compared with a pure polymer.
- Increasing the raster width at a constant layer height of 0.15 mm, leads to a decline in thermal conductivity, which reaches reduction percentages of 65%, 28%, and 25% in x , y , and z directions, respectively, at a raster width in the layer of 0.8 mm.
- Decreasing the fill ratio for the samples with cross-hatched layer configuration decreases the thermal conductivity in the z -direction which can reach up to 63% at 30% infill ratio compared with 100% infill due to the porosity fraction growth.
- The polymer composite results showed a reasonable increase in the thermal conductivity, particularly for the carbon fiber filler which achieved 26% and 162% in z and y directions, respectively, compared with pure polymer. The second direction achieved a higher percentage due to the shear effect happening during the filament extrusion; this tends to orient the fibers and hence help to produce a connected network of the fibers and boost the material heat transfer capability.

Acknowledgements The authors gratefully acknowledge the support of the Natural Sciences and Engineering Research Council of Canada (NSERC).

Compliance with ethical standards

Conflict of interest On behalf of all authors, the corresponding author states that there is no conflict of interest.

References

1. Ngo IL, Jeon S, Byon C (2016) Thermal conductivity of transparent and flexible polymers containing fillers: a literature review. *Int J Heat Mass Transf* 98:219–226. <https://doi.org/10.1016/j.jhehmasstransfer.2016.02.082>
2. Ning F, Cong W, Hu Y, Wang H (2017) Additive manufacturing of carbon fiber-reinforced plastic composites using fused deposition modeling: Effects of process parameters on tensile properties. *J Compos Mater* 51:451–462. <https://doi.org/10.1177/0021998316646169>
3. Kumar S, Kruth JP (2010) Composites by rapid prototyping technology. *Mater Des* 31(2):850–856. <https://doi.org/10.1016/j.matdes.2009.07.045>
4. De Leon AC, Chen Q, Palaganas NB et al (2016) High performance polymer nanocomposites for additive manufacturing applications. *React Funct Polym* 103:141–155. <https://doi.org/10.1016/j.reactfunctpolym.2016.04.010>
5. Berman B, Zarb FG (2011) 3-D printing: The new industrial revolution I. A multi-faceted technology: 3-D printing. *Bus Horiz* 55:155–162. <https://doi.org/10.1016/j.bushor.2011.11.003>
6. Deepa Y (2014) Fused deposition modeling—a rapid prototyping technique for product cycle time reduction cost effectively in aerospace applications. *IOSR J Mech Civ Eng* 5:62–68
7. Wong KV, Hernandez A (2012) A review of additive manufacturing. *ISRN Mech Eng* 2012:1–10. <https://doi.org/10.5402/2012/208760>
8. Deisenroth DC, Moradi R, Shooshtari AH et al (2017) Review of heat exchangers enabled by polymer and polymer composite additive manufacturing. *Heat Transf Eng*. <https://doi.org/10.1080/01457632.2017.1384280>
9. Jia Y, He H, Geng Y et al (2017) High through-plane thermal conductivity of polymer based product with vertical alignment of graphite flakes achieved via 3D printing. *Compos Sci Technol* 145:55–61. <https://doi.org/10.1016/j.compscitech.2017.03.035>
10. Hymas DM, Arie MA, Singer F, et al (2017) Enhanced air-side heat transfer in an additively manufactured polymer composite heat exchanger, thermal and thermomechanical phenomena in electronic systems (ITherm). 16th IEEE intersociety conference on. IEEE, pp 634–638
11. Kalsoom U, Peristyy A, Nesterenko PN, Paull B (2016) A 3D printable diamond polymer composite: a novel material for fabrication of low cost thermally conducting devices. *RSC Adv* 6:38140–38147. <https://doi.org/10.1039/c6ra05261d>
12. Bakar NSA, Alkahari MR, Boejang H (2010) Analysis on fused deposition modelling performance. *J Zhejiang Univ Sci A* 11:972–977. <https://doi.org/10.1631/jzus.A1001365>
13. Santhakumar J, Maggirwar R (2016) enhancing quality of fused deposition modeling built parts by optimizing the process variables using polycarbonate material. *Inte Sci Press* 9:173–181
14. Turner BN, Gold SA (2015) A review of melt extrusion additive manufacturing processes: II. Materials, dimensional accuracy, and surface roughness. *Rapid Prototyping J* 21:250–261
15. Wu W, Geng P, Li G et al (2015) Influence of layer thickness and raster angle on the mechanical properties of 3D-printed PEEK and a comparative mechanical study between PEEK and ABS. *Materials (Basel)* 8:5834–5846. <https://doi.org/10.3390/ma8095271>
16. Cantrell J, Rohde S, Damiani D et al (2011) Experimental characterization of the mechanical properties of 3D-printed ABS and polycarbonate parts. *Rapid Prototyping Journal* 23(4):811–824. https://doi.org/10.1007/978-3-319-41600-7_11
17. Percoco G, Lavecchia F, Galantucci LM (2012) Compressive properties of FDM rapid prototypes treated with a low cost chemical finishing. *Res J Appl Sci Eng Technol* 4:3838–3842
18. Ashtankar KM, Kuthe AM, Rathour BS (2013) Effect of build orientation on mechanical properties of rapid prototyping (fused deposition modelling) made acrylonitrile butadiene styrene (abs) parts. In: Proceedings of the ASME 2013 international mechanical engineering congress and exposition, pp 1–7
19. Arivazhagan A, Saleem A, Masood SH et al (2014) Study of dynamic mechanical properties of fused deposition modelling processed. *Int J Eng Res Appl* 7:304–312. <https://doi.org/10.3844/ajeassp.2014.304.312>
20. Olivier D, Borros S, Reyes G (2010) Influence of building orientation on failure mechanism and flexural properties of low specimens. *J Mech Sci Technol* 00:1261–1269
21. Jadav RA, Solanki B (2015) Investigation on parameter optimization of fused deposition modeling (FDM) for better mechanical properties—a review. *IJSRD -International J Sci Res Dev* 3:2321–2613
22. Álvarez K, Lagos RF, Aizpun M (2016) Investigating the influence of infill percentage on the mechanical properties of fused deposition modelled ABS parts. *Ing e Investig* 36:110. <https://doi.org/10.15446/ing.investig.v36n3.56610>
23. Nikzad M, Masood SH, Sbarski I (2011) Thermo-mechanical properties of a highly filled polymeric composites for fused

- deposition modeling. *Mater Des* 32(6):3448–3456. <https://doi.org/10.1016/j.matdes.2011.01.056>
24. Nikzad M, Masood SH, Sbarski I, Groth a (2007) Thermo-mechanical properties of a metal-filled polymer composite for fused deposition modelling applications. In: 5th Australas Congr Appl Mech ACAM 1:319–324.
 25. Hwang S, Reyes EI, Sik KM et al (2015) Thermo-mechanical characterization of metal/polymer composite filaments and printing parameter study for fused deposition modeling in the 3D printing process. *J Electron Mater* 44(3):771–777. <https://doi.org/10.1007/s11664-014-3425-6>
 26. Masood SH, Song WQ (2002) Assembly Automation Thermal characteristics of a new metal/polymer material for FDM rapid prototyping process Thermal characteristics of a new metal/polymer material for FDM rapid prototyping process. *Assem Autom Rapid Prototyp J Iss Rapid Prototyp J* 25:309–315. <https://doi.org/10.1108/01445150510626451>
 27. Laureto J, Tomasi J, King JA, Pearce JM (2017) Thermal properties of 3-D printed polylactic acid-metal composites. *Prog Addit Manuf* 2:57–71. <https://doi.org/10.1007/s40964-017-0019-x>
 28. Smith DS, Alzina A, Bourret J et al (2013) Thermal conductivity of porous materials. *J Mater Res* 28:2260–2272. <https://doi.org/10.1557/jmr.2013.179>
 29. Mamunya YP, Davydenko VV, Pissis P, Lebedev EV (2002) Electrical and thermal conductivity of polymers filled with metal powders. *Eur Polym J* 38:1887–1897. [https://doi.org/10.1016/S0014-3057\(02\)00064-2](https://doi.org/10.1016/S0014-3057(02)00064-2)
 30. Landauer R (1952) The electrical resistance of binary metallic mixtures. *J Appl Phys* 23:779–784. <https://doi.org/10.1063/1.1702301>
 31. Shemelya C, De La Rosa A, Torrado AR et al (2017) Anisotropy of thermal conductivity in 3D printed polymer matrix composites for space based cube satellites. *Addit Manuf* 16:186–196. <https://doi.org/10.1016/j.addma.2017.05.012>
 32. Flaata, Tiffaney, Gregory J. Michna TL (2017) Thermal conductivity testing apparatus for 3d printed materials thermal conductivity testing apparatus for 3d printed materials. In: ASME 2017 Heat Transfer Summer Conference. American Society of Mechanical Engineers, pp V002T15A006–V002T15A006
 33. Prajapati H, Ravoori D, Woods RL, Jain A (2018) Measurement of anisotropic thermal conductivity and inter-layer thermal contact resistance in polymer fused deposition modeling (FDM). *Addit Manuf* 21:84–90. <https://doi.org/10.1016/j.addma.2018.02.019>
 34. Shofner ML, Lozano K, Rodríguez-Macías FJ, Barrera EV (2003) Nanofiber-reinforced polymers prepared by fused deposition modeling. *J Appl Polym Sci* 89:3081–3090. <https://doi.org/10.1002/app.12496>
 35. Ibrahim Y, Melenka G, Kempers R (2018) Additive manufacturing of continuous wire polymer composites. *Manuf Lett* 16:49–51. <https://doi.org/10.1016/j.mfglet.2018.04.001>
 36. Ibrahim Y, Melenka G, Kempers R (2018) Fabrication and tensile testing of 3d printed continuous wire polymer composites. *Rapid Prototyp J*. <https://doi.org/10.1108/RPJ-11-2017-0222>
 37. Yang C, Tian X, Liu T et al (2017) 3D printing for continuous fiber reinforced thermoplastic composites: mechanism. *Rapid Prototyp J* 23(1):209–215. <https://doi.org/10.1108/RPJ-08-2015-0098>
 38. Zhang F, Ma G, Tan Y (2017) The nozzle structure design and analysis for continuous carbon fiber composite 3D printing. *Adv Eng Res* 136:193–199
 39. Tian X, Liu T, Yang C et al (2016) Interface and performance of 3D printed continuous carbon fiber reinforced PLA composites. *Compos Part A Appl Sci Manuf* 88:198–205. <https://doi.org/10.1016/j.compositesa.2016.05.032>
 40. Masaki N, Ueda M, Todoroki A, Hirano Y, Matsuzaki R (2014) 3D printing of continuous fiber reinforced plastic. *Proc Soc Adv Mater and Process Eng* 45:187–196
 41. Dizon JRC, Espera AH, Chen Q, Advincula RC (2018) Mechanical characterization of 3D-printed polymers. *Addit Manuf* 20:44–67. <https://doi.org/10.1016/j.addma.2017.12.002>
 42. Ng HY, Lu X, Lau SK (2005) Thermal conductivity of boron nitride-filled thermoplastics: effect of filler characteristics and composite processing conditions. *Polym Compos* 26:778–790. <https://doi.org/10.1002/pc.20151>
 43. Kempers R, Kolodner P, Lyons A, Robinson AJ (2009) A high-precision apparatus for the characterization of thermal interface materials. *Rev Sci Instrum* 80(9):095111. <https://doi.org/10.1063/1.3193715>
 44. ASTM C177 (2013) Standard test method for steady-state heat flux measurements and thermal transmission properties by means of the guarded-hot-plate. *ASTM Int*. <https://doi.org/10.1520/C0177-13.2>
 45. Kline SJ, McClintock FA (1953) Describing uncertainties in single-sample experiments. *Mech Eng* 75(1):3–8
 46. ANSYS (2015) ANSYS Fluent Theory Guide. ANSYS 16 Doc. 15317:80
 47. Specialty Filament | ROBO 3D. <https://robo3d.com/collections/filament-exotic>. Accessed 7 Aug 2018
 48. Proto-pasta 3D Printer Filament Made by the Makers at ProtoPlant–ProtoPlant, makers of Proto-pasta. <https://www.proto-pasta.com/>. Accessed 7 Aug 2018
 49. Dehdari Ebrahimi N, Ju YS (2018) Thermal conductivity of sintered copper samples prepared using 3D printing-compatible polymer composite filaments. *Addit Manuf* 24:479–485. <https://doi.org/10.1016/j.addma.2018.10.025>
 50. Gibson MA, Mykulowycz NM, Shim J et al (2018) 3D printing metals like thermoplastics: fused filament fabrication of metallic glasses. *Mater Today* 21:697–702. <https://doi.org/10.1016/j.matto.2018.07.001>